Molecular Aggregates Associated THz Coherent Vibrations Contribute to Enhancements of Emission Efficiencies

Yu-Chen Wei
National Taiwan University https://orcid.org/0000-0003-4120-0685
Bo-Han Chen
National Tsing Hua University
Ren-Siang Ye
National Tsing Hua University
Hsing-Wei Huang
National Tsing Hua University
Jia-Xuan Su
National Tsing Hua University
Kai Chen
Victoria University of Wellington
Lian-Yan Hsu
National Taiwan University
Yun Chi
National Tsing Hua University
Chih-Hsuan Lu
Shang-Da Yang
National Tsing Hua University
Pi-Tai Chou (chop@ntu.edu.tw)
National Taiwan University https://orcid.org/0000-0002-8925-7747

Article

Keywords:

Posted Date: October 6th, 2022

DOI: https://doi.org/10.21203/rs.3.rs-2118385/v1

Molecular Aggregates Associated THz Coherent Vibrations Contribute to Enhancements of Emission Efficiencies

Yu-Chen Wei[1,6†], Bo-Han Chen[2,†], Ren-Siang Ye[2], Hsing-Wei Huang[2], Jia-Xuan Su[2], Kai Chen[3,4,5], Lian-Yan Hsu[1,6], Yun Chi[7,*], Chih-Hsuan Lu[2,*], Shang-Da Yang[2,*], Pi-Tai Chou[1,*]

[1] Department of Chemistry, National Taiwan University, Taipei 10617, Taiwan; E-mail: chop@ntu.edu.tw

[2] Institute of Photonics Technologies, National Tsing Hua University, Hsinchu 30013, Taiwan; E-mail: lzch2000@hotmail.com; shangda@ee.nthu.edu.tw

[3] Robinson Research Institute, Faculty of Engineering, Victoria University of Wellington, Wellington 6012, New Zealand

[4] The Dodd-Walls Centre for Photonic and Quantum Technologies, Dunedin 9016, New Zealand

[5] MacDiarmid Institute for Advanced Materials and Nanotechnology, Wellington, 6010 New Zealand

[6] Institute of Atomic and Molecular Sciences, Academia Sinica, Taipei 10617, Taiwan

[7] Department of Materials Science and Engineering, Department of Chemistry, and Center of Super-Diamond and Advanced Films (COSDAF), City University of Hong Kong, Hong Kong SAR; E-mail: yunchi@cityu.edu.hk

†These authors contributed equally

The control of excited-state vibrational and electronic energy flows in molecular solids has a considerable impact on the performance of optoelectronic devices. In this study, we applied a novel ultrafast pump-probe system with 3.2 fs resolution to demonstrate that the aggregated Pt(II) complex 4H, an efficient near-infrared emitter, exhibits prominent single-mode vibrational coherence (VC) with a frequency of 32 cm^{-1} (~ 0.96 THz) in the excited state. This single-mode VC is associated with the collective out-of-plane motions induced by intermolecular metal-metal-to-ligand charge transfer transitions, which occur through ultrafast intersystem crossings with lifetimes of 150 fs. Similar single-mode VC characteristics were observed in analogues of 4H and other Pt(II) complexes with intense NIR emission. The conservation of single-mode VC enables excited-state deactivation to proceed along low-frequency coordinates, which contributes to the

suppression of nonradiative decay rates and causes highly intense near-infrared emission in aggregated Pt(II) complexes. These novel results highlight the importance of VC in understanding nonradiative processes, elucidating the foundations of VC in molecular solid, which serve as a benchmark for evolving the device performance.

Quantum coherence has attracted broad interest due to its potential role in influencing photophysical and photochemical processes[1-13] and in energy-conversion applications such as photocatalysis, photovoltaics and luminescent materials. In polyatomic systems ranging from small molecules to proteins, vibrational coherence (VC), a quantum coherence that reflects vibrational degrees of freedom, occurs upon electronic excitation and can provide insights into excited-state relaxation or reaction pathways. To prevent significant decoherence processes, the dynamics of VC are usually studied in the gaseous or solution phases.[7, 14, 15] Recently, due to rapid advances in materials science, VC in the solid phase has been investigated, and the impact of VC on optoelectronic devices has received considerable attention.[16-25] Several studies have proposed that VC may assist photoinduced charge separation in photovoltaic materials,[16, 18, 25, 26] although the correlation between VC-assisted charge separation and device performance is still unknown.[17, 27] Despite fundamental and technical difficulties, this emerging field has considerable potential and various unexplored topics. In this study, we aim to explore the advantages of VC in molecular solids to reveal new material properties. Moreover, the underlying mechanisms are expected to enhance practical applications of these materials.

Here, we focus on the ultrafast dynamics of the self-assembled Pt(II) complex **4H** (**Fig. 1a**) in a solid film, which has been reported to exhibit highly intense near-infrared (NIR) photoluminescence and electroluminescence at > 830 nm.[28] We utilized transient absorption spectroscopy (TAS) driven by a ytterbium-based multiple plate compression (MPC) light source,[29-31] which provides ultrafine and adjustable time resolution up to 3.2 fs. Based on the proposed MPC-TAS system, we acquired comprehensive pulse-duration and excitation-wavelength dependent TA measurements and verified a single-mode VC at 32 cm^{-1} in the **4H** solid film that was conserved during ultrafast intersystem crossings. Importantly, similar single-mode VC patterns were observed in analogues and other Pt(II) complexes in thin films that were correlated with anomalously intense NIR emissions in the self-assembled Pt(II) complexes.[28, 32-34] This finding, as well as additional computational results, led us to propose that the conservation of single-mode VC contributes to the suppression of nonradiative decay rates by reducing vibration-associated excited-state deactivation. Thus, this study provides a novel perspective on

VC that may encourage investigations on the correlation among vibrational coherence, exciton delocalization and exciton-vibration coupling in molecular solids and the effects on device performance.

Results

System. The aggregation of Pt(II) complexes anchored with various electron donor-acceptor chelates has become one of the most promising classes of NIR emitters for organic light-emitting diodes (OLEDs), with a maximum emission in the 700-1000 nm region and a photoluminescent quantum yield (PLQY) greater than 10% in thin films.[28, 32-34] This efficient and redshifted optical transition arises due to self-assembly, i.e., the formation of well-aligned molecular packing structures. According to previous reports, as shown in **Fig. 1a**, the intermolecular distance along the *c* axis for this class of Pt(II) complexes is extremely short, i.e., approximately 0.42 nm, significantly increasing intermolecular interactions and resulting in redshifted emissions.[28] In this study, we analysed a prototypical aggregated **4H** exhibiting intense emissions, with the peak centred at 866 nm (**Fig. 1a** and **1b**).[28] To elucidate the characteristics of the electronic transition upon aggregation, we performed density functional theory (DFT) calculations on tetrameric **4H**, and the initial packing alignment is determined according to the grazing incidence X-ray diffraction (GIXD) structure along the *c* axis.[27] Detailed information on the DFT calculation is provided in the Methods section. An analysis of the natural transition orbital shows the dominant intermolecular metal-metal-to-ligand charge transfer (MMLCT) transition (**Fig. 1c**), which is common in dimeric and oligomeric Pt complexes.[4, 35-40] As mentioned in previous studies,[28] the oblique packing structure decreases the wavefunction overlaps between the dz^2 orbitals of central Pt(II) atoms, leading to a reduced probability density for central Pt(II) atoms in the particle transition orbital. Note that the number of the simulated aggregated **4H** (N = 4) is similar to the observed exciton delocalization length in experimental approaches (N = 5-6),[28] validating our calculation results.

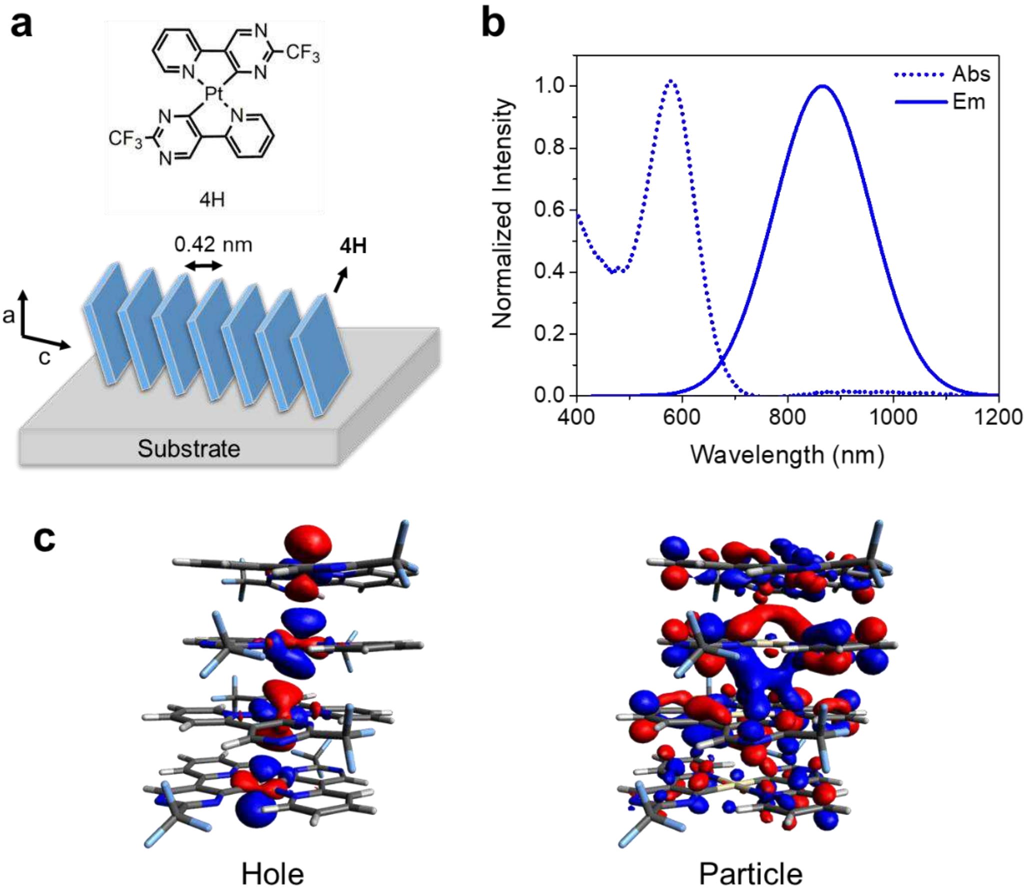

Figure 1 ｜ Aggregated Pt(II) complex 4H in a thin film. (a) Molecular structure and schematic illustration of packing alignments. The distance is adopted from a grazing-incidence X-ray diffraction experiment.[28] (b) Steady-state absorption (dotted line) and emission (solid line) spectra in a thin film at RT. (c) Natural transition orbitals of tetrameric **4H** with an S_0 equilibrium geometry. The eigenvalues of the hole and particle are set to 0.83.

Ultrafast dynamics and vibrational coherence in aggregated 4H. To probe the ultrafast dynamics of aggregated **4H**, we built a multiple plate compression (MPC) system to generate an intense and coherent supercontinuum spanning from 550 nm to 950 nm (**Figs. 2a** and S1). Detailed information on the MPC system is provided in the Methods section. Spectral filtering and dispersion compensation methods can be applied to tune the pulse duration between 3.2 fs and 115 fs. In addition, the central excitation wavelength can be tuned between 450~980 nm by using additional harmonic generation and tunable colour filters. This approach allows us to vary the time resolution and excitation wavelength in the transient absorption spectroscopy (TAS) system. The pulse durations are characterized by polarization-gating frequency-resolved optical gating[41, 42] (PG-FROG) at the sample position (Figs. S1-S4). Based on the MPC-TAS technique, the transient absorption (TA) spectra for a **4H** solid film with a 3.2 fs excitation pulse duration were measured **(Fig. 2b)**. In a 250 fs time window, the positive transmission difference corresponds to ground-state bleaching (GSB) from the singlet ground state (S_0) to the first singlet excited state (S_1), and the negative transmission difference corresponds to excited-state absorption (ESA) from S_1 to a higher singlet state (S_n). The GSB is verified by the central excitation wavelength dependence of the TA measurements, demonstrating the matching spectral distribution between the GSB signal and the excitation spectral range (Fig. S5). In addition, the excitation-wavelength-dependent GSB in Figs. S5 and S6, which is associated with transient spectral hole burning,[43] reveals the considerable inhomogeneity of the aggregated **4H**. After 250 fs, the drastic change in the TA spectrum indicates the occurrence of a new process, and the corresponding assignments can be divided into two parts. First, according to the steady-state absorption spectra (**Fig. 1b**), the positive $\Delta T/T$ centred at 625 nm and 800 nm are assigned as GSB, and the spectral change in the GSB signal may be related to energy migration processes.[43] Then, we determine that the ESA centred at 700 nm corresponds to populations in the triplet state (T_n) due to the substantial Pt(II) atom-enhanced spin-orbit coupling (SOC) between S_1 and T_n (Tables S1 and S2). Moreover, we deduce that the first populated triplet state T_n is T_1, which is near S_1, due to the overlapping onset energy between the steady-state absorption ($S_0 \rightarrow S_1$) and emission peaks (mainly $T_1 \rightarrow S_0$) (**Fig. 1b**) and the calculated energy diagram (Figs. S7 and S8).

Based on the above assignments, the considerable spectral change after 250 fs indicates intersystem crossing (ISC) from S_1 to T_1 with a time constant τ_{ISC} of 150 fs. Importantly, the validity of τ_{ISC} is confirmed because the temporal evolution in the TA spectra remains essentially constant when the pump pulse duration changes from 3.2 fs to 115 fs (Figs. S9 and S10). Note that the remaining ESA centred at 575 nm indicates that the populations in S_1 are partially transferred to the T_1 state and that the dynamics reach pseudo equilibrium. These results indicate a small singlet-triplet energy gap between S_1 and T_1, which is consistent with the calculated electronic energy levels (Figs. S7 and S8).

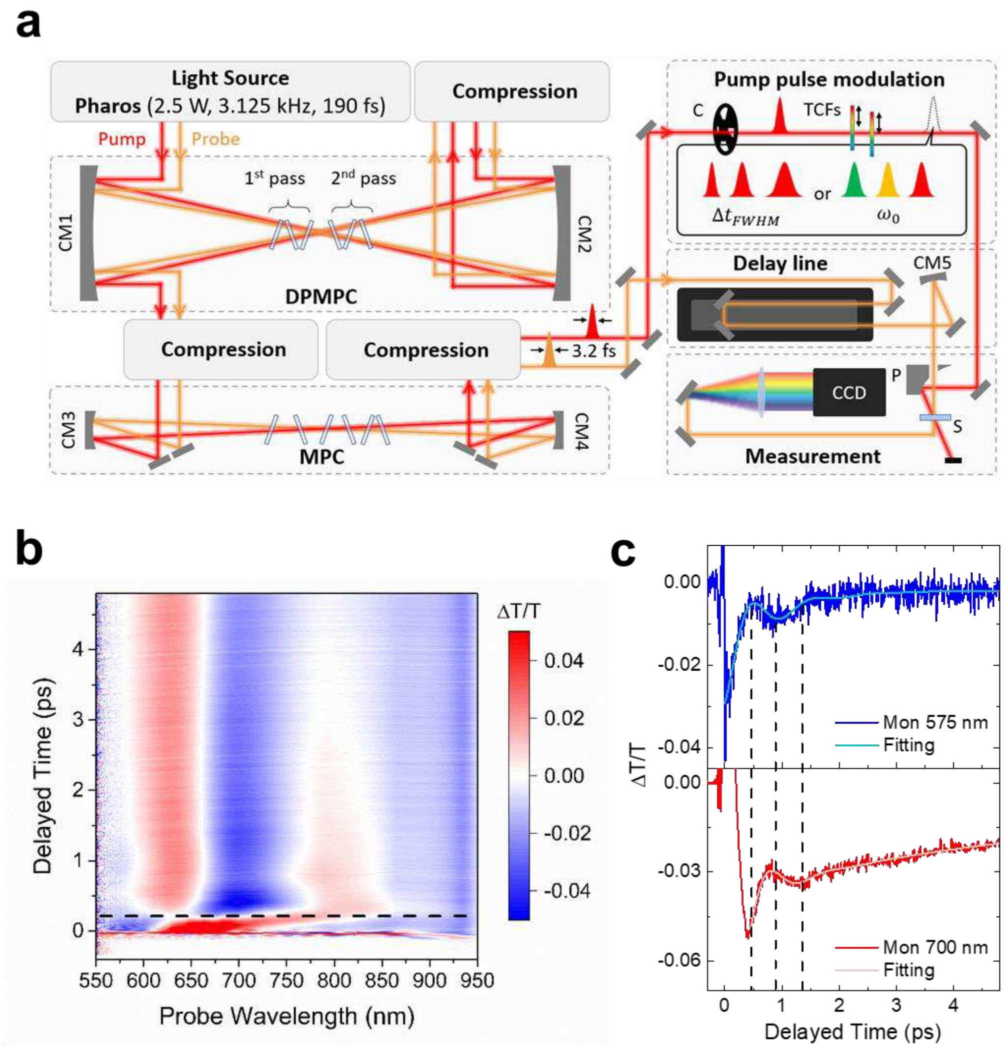

Figure 2 ｜Ultrafast dynamics of vibrational coherence in aggregated 4H. (a) Schematic setup of the MPC-TAS system. The spectral bandwidth is spanned over one octave using multiple stages of different MPC modules,[29, 44] and the shortest pulse duration is 3.2 fs. The pump pulse is modulated by a mechanical chopper and the pulse duration, and the excitation bandwidth can be arbitrarily adjusted by two tunable colour filters. The temporal overlap between the pump and probe pulses is scanned by a delay line system, and the transient transmission spectra are measured by our designed spectrometer. CM1~CM5: concave mirrors, C: chopper, TCFs: tunable colour filters, P: off-axis parabolic mirror, S: sample. (b) Transient absorption spectra of aggregated **4H** measured by a 3.2 fs pump pulse at RT. ΔT/T indicates the transmission difference. The black dashed line represents the delay time at 250 fs. (c) Time traces of (b) monitored at selected wavelengths, indicating the singlet-state ESA (575 nm) and triplet-state ESA (700 nm). The amplitude modulations in the singlet-state ESA and triplet-state ESA oscillate with a similar frequency of 32 cm^{-1}.

Notably, the 32 cm^{-1} (~0.96 THz) oscillatory signals arising in the ESAs centred at 575 nm and 700 nm are of particular interest because they represent single-mode VC in the S_1 and T_1 states, respectively (**Fig. 2b** and **2c**). In addition, **Fig. 2c** shows that single-mode VC is conserved during the ISC process, resulting in out-of-phase population dynamics in S_1 and T_1. Note that S_1 and T_1 have similar dephasing lifetimes (τ_d ~ 534 fs), which supports our proposed mechanism because the population dynamics in S_1 and T_1 both reached pseudo equilibrium. It is worth noting that the oscillatory signals are not caused by the impulsive Raman responses due to the lack of an oscillatory signal in the TA measurement with off-resonance pumping (Fig. S5e). In addition, the assignment of single-mode VC is supported by the fast Fourier transform (FFT) results, which show a lack of significant FFT signals as the frequency exceeds 50 cm^{-1} (Fig. S11). Moreover, an analysis of the wavelength-resolved FFT shows that the oscillatory frequency is independent of the probed wavelength, proving that the 32 cm^{-1} oscillatory signals are not caused by the strain pulse propagation.[45, 46] Importantly, similar patterns occur in **4H** analogues and other Pt(II) complexes such as Pt(fprpz)$_2$, 4Me, 4tBu, DR and MeDR in thin films (**Figs. 3a** and S12), which have been reported to exhibit highly intensive NIR emissions.[28, 32-34] Thus, the results demonstrate the ubiquity of single-mode THz VC in solid-state Pt(II) aggregates. Interestingly, **Fig. 3b** shows that the VC frequencies of these Pt(II) complexes are inversely correlated with the delocalization length, revealing that longer delocalization lengths contribute to slower coherent vibrational motions (**Fig. 3c**). Incidentally, the delocalization lengths are determined by the relation of one-exciton to biexiton transition energy and the delocalization lengths.[28, 34] Note that the delocalization length dependence of VC frequency agrees with the concept that exciton delocalization contributes to the partitioning of vibrational reorganization energy.[28]

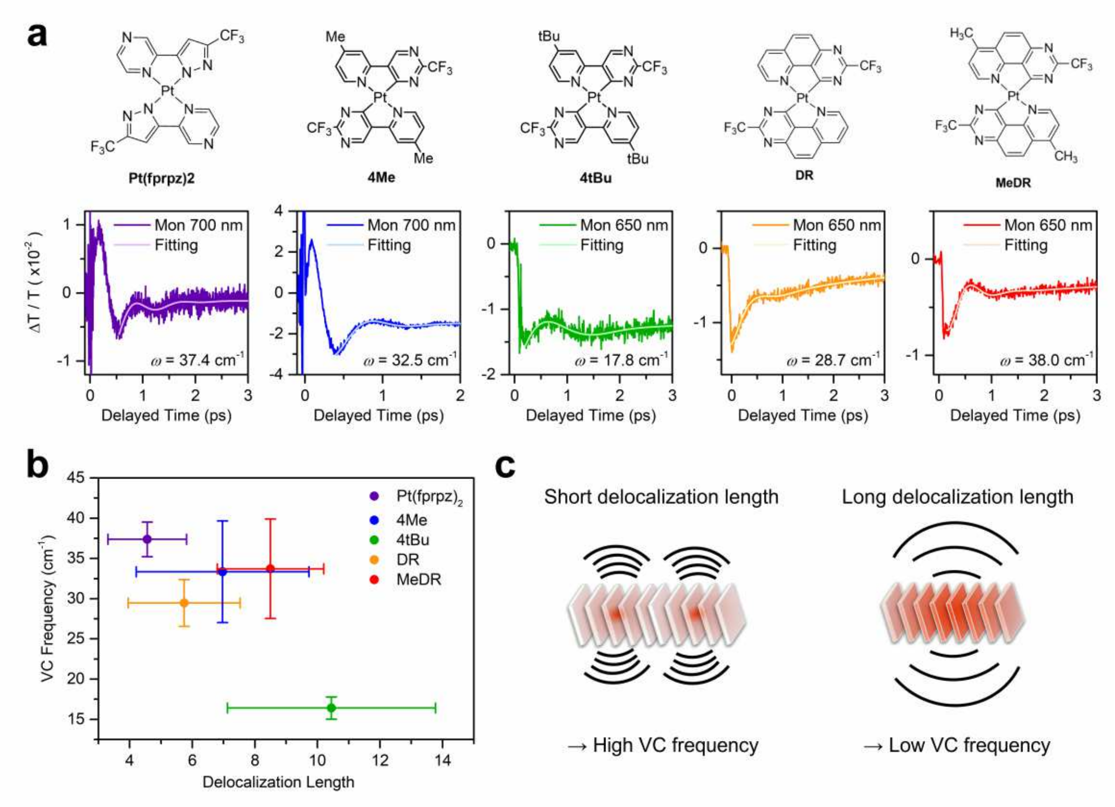

Figure 3 │ Correlation of VC frequency and Delocalization lengths in 4H analogues and other Pt(II) complexes in thin films. (a) Time traces of transient absorption spectra of various aggregate Pt complexes in thin film with 3.2 fs pumping pulse at room temperature. The frequency ω indicates the single mode VC. (b) Delocalization length dependence of VC frequency. The deviation of delocalization lengths arises from the full-width-at-half-maximum of the one-exciton to biexciton excited-state absorption peak. The deviation of VC frequencies results from the fitting results of different probed wavelengths. (c) Schematic illustration of suppressing VC frequency via elongation of delocalization length. The red shades represent the delocalization lengths.

To investigate the nuclear displacements of the 32 cm^{-1} VC in **4H**, we calculate the vibrational normal modes in the S_0 state and demonstrate that normal modes with frequencies close to 32 cm^{-1} are associated with collective out-of-plane motions **(Fig. 4**). Notably, due to the slow structural relaxation induced by the 32 cm^{-1} VC, it is reasonable to assume that the molecular geometry resembles the S_0 equilibrium geometry in the observed time range. Among the three normal modes depicted in **Fig. 4**, the Pt(II) atoms are displaced mainly along the Pt–Pt direction (*c* axis) in the 36.6 cm^{-1} normal mode. In contrast, the Pt(II) atoms in the 28.8 cm^{-1} and 33.7 cm^{-1} normal modes are displaced mainly along the *a* and *b* axes, respectively, which differs from the nuclear motions of VC in reported dimeric and oligomeric Pt(II) complexes.[4, 35-40] The results indicate that the Pt–Pt stretching mode (36.6 cm^{-1}) and in-plane shearing modes (28.8 cm^{-1} and 33.7 cm^{-1}) are involved in the VC induced by the intermolecular MMLCT transition process.

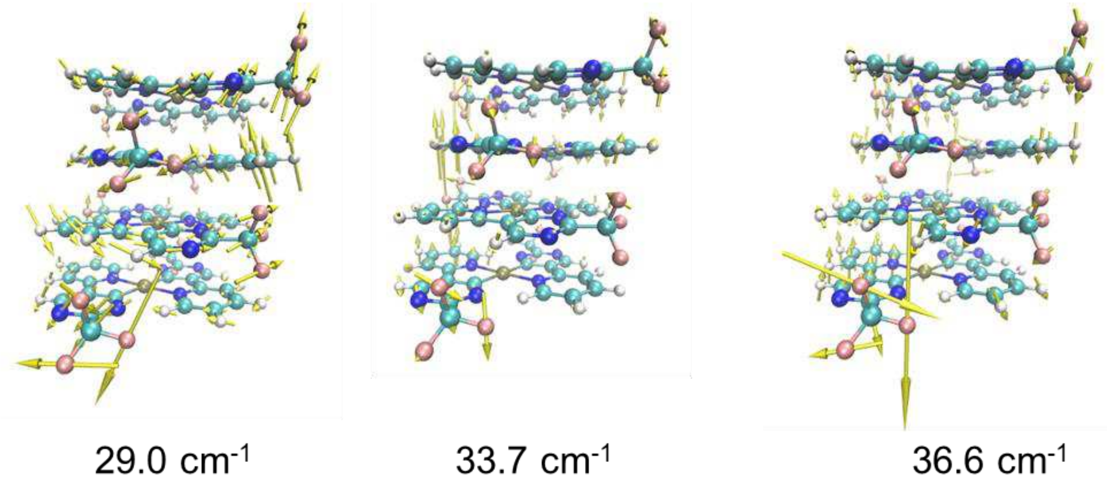

Figure 4 │ Possible normal mode displacements of the observed VC in the optimized ground-state geometry. The yellow vectors indicate the nuclear displacements.

To explore the formation mechanism of the 32 cm^{-1} single-mode VC, we perform TA measurements at different central excitation wavelengths λ_0 (Fig. S5). The results show that the 32 cm^{-1} single-mode VC occurs during S_0-S_1 electronic excitation (λ_0 = 600 or 650 nm) but disappears during high electronic excitation (λ_0 = 460 nm), revealing that the 32 cm^{-1} single-mode VC is mainly associated with S_0-S_1 MMLCT absorption. To validate this inference, we calculate the nuclear displacement (Huang-Rhys (HR) factor) between S_0 and S_1 since VC signals are correlated with the amplitudes of HR factors (Fig. S13).[13, 47, 48] The results show that nuclear displacements at low vibrational frequencies (< 50 cm^{-1}) are considerably greater than those at high vibrational frequencies. Thus, we deduce that the 32 cm^{-1} single-mode VC arises due to the large nuclear displacements between the ground-state and excited-state geometries at equilibrium. We note that the 32 cm^{-1} single-mode VC is not typically associated with ISC processes in our system. First, according to the Franck-Condon principle, the considerable disparity between the time scales of the ISC lifetime (τ_{ISC} = 150 fs) and VC period (~ 1.0 ps) indicates that the nuclear dynamics decouples with ISC processes. In addition, the FFT analysis shows the negligible contributions of frequencies > 150 cm^{-1} before and after the ISC process (Fig. S14), thereby revealing that the ISC process does not filter out VC frequencies in our system. In summary, the VC in our system does not reveal the reaction coordinate of the ISC process and instead elucidates the vibrational relaxation pathway between the ground-state and excited-state equilibrium geometries.

Based on the above experimental and calculation results, we summarize the ultrafast dynamics of VC in aggregated **4H** (**Fig. 5**) as follows: upon photoexcitation, the dynamics evolve mainly along the normal mode with a frequency of 32 cm^{-1}, leading to the formation of a 32 cm^{-1} oscillatory signal. Next, the 32 cm^{-1} VC is transferred from the S$_1$ state to the T$_1$ state through an ultrafast ISC process with a τ_{ISC} of 150 fs. In addition, the small singlet (S$_1$)-triplet (T$_1$) energy gap results in pseudo equilibrium between the S$_1$ and T$_1$ states. After 1 ps (~ one VC period), the VC in the S$_1$ and T$_1$ states gradually disappears with a similar dephasing lifetime (τ_d ~ 534 fs).

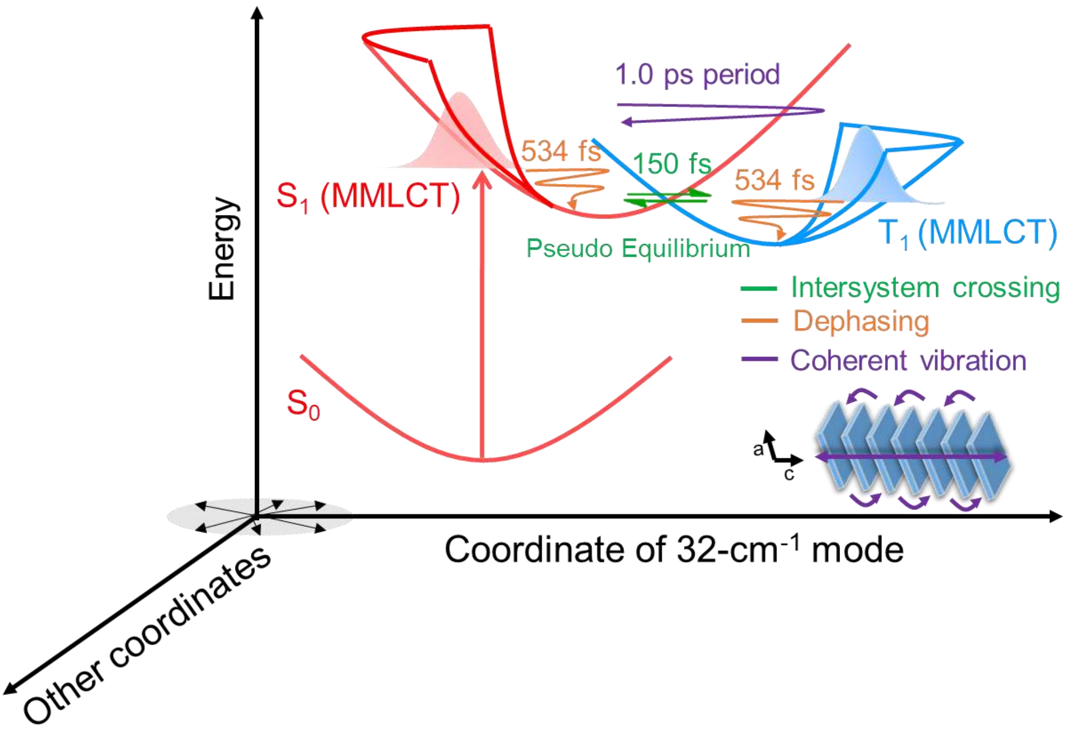

Figure 5 │ Schematic representations of the key ultrafast dynamic processes of VC in aggregated 4H. The red arrow represents photoexcitation. The green lines indicate intersystem crossing (ISC). The orange arrows represent the dephasing processes in the S$_1$ and T$_1$ states. The bottom-right inset illustrates the direction of the 32 cm^{-1} coherent vibrational mode.

Correlation between low-frequency VC and nonradiative decay rates. To clarify the relation between vibrations and nonradiative processes, we introduce the theory of nonradiative rates k_{nr} derived by Englman and Jortner. Here, we focus on nonradiative processes caused by vibronic coupling. Therefore, in the strong vibronic coupling regime shown in Fig. S13 (total HR factor >> 1), k_{nr} can be expressed as[49]

$$k_{\mathrm{nr}} = \frac{C^2}{\hbar}\sqrt{\frac{2\pi}{\lambda k_B T_{\mathrm{eff}}}}\exp\left[-\frac{(\Delta E - \lambda)^2}{4\lambda k_B T_{\mathrm{eff}}}\right], \tag{1}$$

where $T_{\mathrm{eff}} = \frac{1}{2}\hbar\bar{\omega}\coth(\frac{\hbar\bar{\omega}}{2kT})$ corresponds to the effective temperature, $\bar{\omega} = \sum_j S_j\omega_j / \sum_j S_j$ is the mean vibrational frequency weighted by the HR factor of each normal mode S_j, C is the effective electronic coupling strength, ΔE is the energy gap between two electronic states and λ is the total vibrational reorganization energy. The validity of Eq. 1 is discussed in the Methods section. We applied Eq. 1 to quantitatively analyse the $\bar{\omega}$ dependence of k_{nr} in our system (**Fig. 6a**). Note that C is adopted from the calculated SOC between T_1 and S_0, and ΔE is determined according to the experimental emission peak (866 nm). Given these parameters, **Fig. 6a** shows that a low value of $\bar{\omega}$ suppresses k_{nr}. Comparing the simulated (blue, red and green lines) and experimental k_{nr} results (black solid circle) in **Fig. 6a**, we note that the intersections of the abscissa are smaller than the frequencies of C=C ligand vibrations (~1600 cm^{-1}) and C-H vibrations (~3000 cm^{-1}), which reveals that nonradiative processes in our system are substantially suppressed by low-frequency vibrational deactivation pathways. Therefore, assuming that intramolecular vibrational energy redistribution (IVR) processes between the 32 cm^{-1} coordinate and other coordinates can be neglected due to their low frequency,[50] the 32 cm^{-1} single-mode VC may contribute to the suppression of nonradiative processes governed by the energy-gap law, leading to high PLQY in the NIR region. The detailed effects of VC on the suppression of k_{nr} can be summarized as follows. First, the single-mode characteristics reveal that the excited-state populations evolve mainly along the 32 cm^{-1} nuclear coordinate, which results in a low $\bar{\omega}$ (see T_{eff} of eq. (1)) Moreover, the 32 cm^{-1} VC associated with intermolecular displacements suppresses IVR processes from the 32 cm^{-1} coordinate and high-frequency intramolecular displacements due to orthogonality.

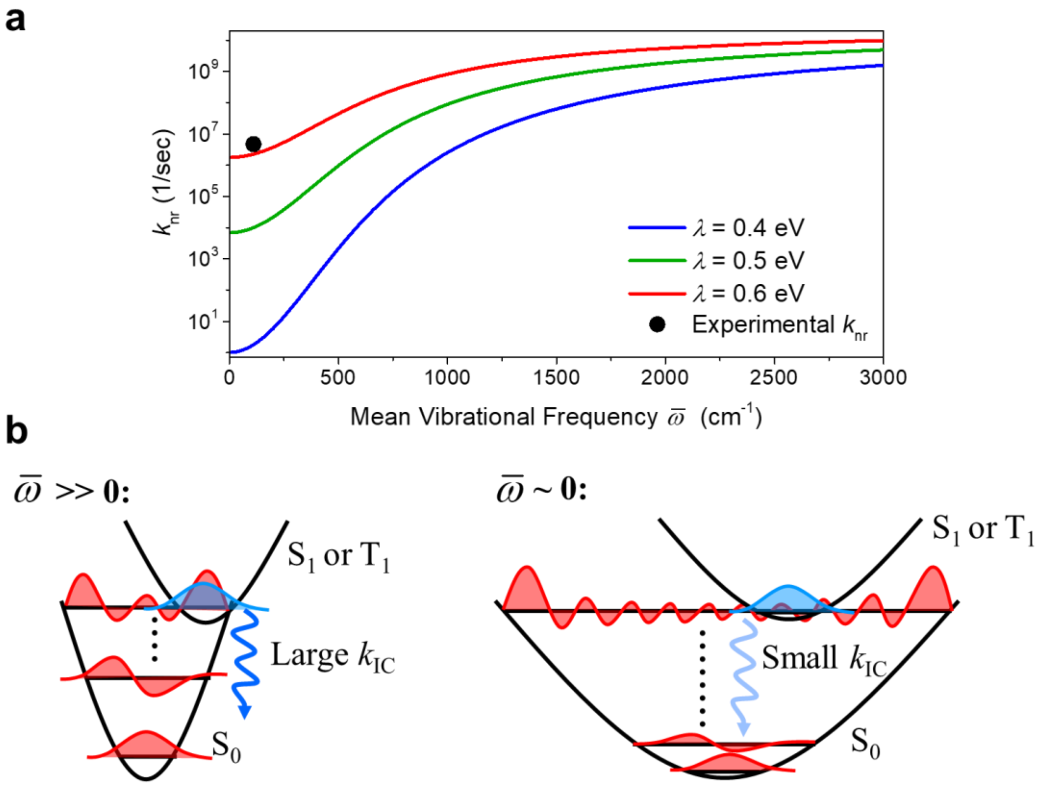

Figure 6 | Effects of the mean vibrational frequency on nonradiative rates. (a) ϖ dependence of nonradiative decay rates k_{nr} for different vibrational reorganization energies λ. Please see the text for the parameter values used in Eq. (1). The black solid circle represents the experimental value of the nonradiative rate.[28] The experimental ϖ = 111 cm^{-1} is estimated according to the calculated HR factor (Fig. S14). (b) Schematic illustration of the nonradiative processes for different mean vibrational frequencies (ϖ). The red and blue shaded areas represent the vibrational wavefunctions in the ground and excited states, respectively. The intensity of the blue wagging arrows represents the amplitude of k_{nr}.

To generalize the concept of k_{nr} suppression by decreasing ϖ, we provide a physical overview of the ϖ dependence of k_{nr} in **Fig. 6b**. For $\varpi \gg 0$, severe nonradiative processes occur due to significant Franck-Condon overlaps among vibrational states between excited states (S_1 or T_1) and S_0. For $\varpi \approx 0$, the small Franck-Condon overlaps inhibit nonradiative processes. In other words, a small value of ϖ reduces the characteristic energy gap where k_{nr} can increase, thereby reducing nonradiative processes in the NIR region and essentially overcoming the energy-gap law. Thus, we conclude that k_{nr} can be effectively suppressed if one of the excited-state deactivation processes occurs along the low-frequency vibrational coordinate axis. A similar concept has been realized through deuterium substitutions, which decrease nonradiative decay rates caused by high-frequency C-H vibrations.[34, 51-53]

Conclusion

In this study, we investigate the VC dynamics in the aggregated Pt(II) complex **4H** and the suppression of nonradiative decay rates according to low-frequency VC. The significance of this work can be summarized as follows. First, we applied versatile pump-pulse modulations in the proposed MPC-TAS system to observe and characterize the 32 cm^{-1} single-mode VC and 150 fs ultrafast ISC processes in aggregated **4H**. This experiment confirmed for the first time that the MPC system can modulate pulse duration and bandwidth in transient absorption spectroscopy, thus providing an omnidirectional platform for adjusting pumping and probing pulses. Moreover, the 32 cm^{-1} single-mode VC is associated with collective out-of-plane vibrations that arise due to the substantial vibrational displacements along the low-frequency coordinates between S_0 and S_1 (MMLCT transition). In addition, the 32 cm^{-1} VC is expected to exhibit THz responses in THz spectroscopy measurements,[54, 55] which should be investigated in future applications. Furthermore, based on the similar VC patterns in **4H**, its analogues and other Pt(II) complexes, we suggest that low-frequency VC contributes to the suppression of nonradiative rates by decreasing the mean vibrational frequency, which may account for the high NIR PLQY in aggregated Pt(II) complexes. The concept of nonradiative decay suppression can be viewed as reducing the threshold of the energy gap where the effects of the energy-gap law are significant (particularly in the NIR region). Finally, the results indicate that well-aligned molecular solids with substantial intermolecular charge-transfer transitions are promising candidates for NIR luminescent materials since they tend to be associated with characteristic low-frequency VC. Moreover, the VC frequencies or mean vibrational frequencies can be used as benchmarks to predict the nonradiative decay rates and design efficient optoelectronic devices. Thus, this study not only provides a new perspective on VC in molecular aggregates but also demonstrates the correlation between VC and emission efficiency, potentially improving device performance.

References

1. Scholes GD, Fleming GR, Chen LX, Aspuru-Guzik A, Buchleitner A, Coker DF, *et al.* Using coherence to enhance function in chemical and biophysical systems. *Nature* **543** 647-656 (2017).

2. Schultz JD, Shin JY, Chen M, O'Connor JP, Young RM, Ratner MA*, et al.*

Influence of Vibronic Coupling on Ultrafast Singlet Fission in a Linear Terrylenediimide Dimer. *J. Am. Chem. Soc.* **143** 2049-2058 (2021).

3. Gueye M, Manathunga M, Agathangelou D, Orozco Y, Paolino M, Fusi S*, et al.* Engineering the vibrational coherence of vision into a synthetic molecular device. *Nat. Commun.* **9** 313 (2018).

4. Monni R, Capano G, Auböck G, Gray HB, Vlček A, Tavernelli I*, et al.* Vibrational coherence transfer in the ultrafast intersystem crossing of a diplatinum complex in solution. *Proc. Natl. Acad. Sci. U.S.A.* **115** E6396-E6403 (2018).

5. Yoneda Y, Sotome H, Mathew R, Lakshmanna YA, Miyasaka H. Non-condon Effect on Ultrafast Excited-State Intramolecular Proton Transfer. *J. Phys. Chem. A* **124** 265-271 (2020).

6. Takeuchi S, Ruhman S, Tsuneda T, Chiba M, Taketsugu T, Tahara T. Spectroscopic Tracking of Structural Evolution in Ultrafast Stilbene Photoisomerization. *Science* **322** 1073-1077 (2008).

7. Dean JC, Scholes GD. Coherence Spectroscopy in the Condensed Phase: Insights into Molecular Structure, Environment, and Interactions. *Acc. Chem. Res.* **50** 2746-2755 (2017).

8. Kruppa SV, Bäppler F, Holzer C, Klopper W, Diller R, Riehn C. Vibrational Coherence Controls Molecular Fragmentation: Ultrafast Photodynamics of the [Ag2Cl]+ Scaffold. *J. Phys. Chem. Lett.* **9** 804-810 (2018).

9. Jaiswal VK, Kabaciński P, Nogueira de Faria BE, Gentile M, de Paula AM, Borrego-Varillas R*, et al.* Environment-Driven Coherent Population Transfer Governs the Ultrafast Photophysics of Tryptophan. *J. Am. Chem. Soc.* **144** 12884-12892 (2022).

10. Aster A, Bornhof A-B, Sakai N, Matile S, Vauthey E. Lifetime Broadening and Impulsive Generation of Vibrational Coherence Triggered by Ultrafast Electron Transfer. *J. Phys. Chem. Lett.* **12** 1052-1057 (2021).

11. Rafiq S, Fu B, Kudisch B, Scholes GD. Interplay of vibrational wavepackets during an ultrafast electron transfer reaction. *Nat. Chem.* **13** 70-76 (2021).

12. Paulus BC, Adelman SL, Jamula Lindsey L, McCusker James K. Leveraging excited-state coherence for synthetic control of ultrafast dynamics. *Nature* **582** 214-218 (2020).

13. Yoneda Y, Kudisch B, Rafiq S, Maiuri M, Nagasawa Y, Scholes GD*, et al.* Vibrational Dephasing along the Reaction Coordinate of an Electron Transfer Reaction. *J. Am. Chem. Soc.* **143** 14511-14522 (2021).

14. Zewail AH. Femtochemistry: Atomic-Scale Dynamics of the Chemical Bond Using Ultrafast Lasers (Nobel Lecture). *Angew. Chem. Int. Ed.* **39** 2586-2631 (2000).

15. Chergui M. Ultrafast Photophysics of Transition Metal Complexes. *Acc. Chem. Res.* **48** 801-808 (2015).

16. Bian Q, Ma F, Chen S, Wei Q, Su X, Buyanova IA*, et al.* Vibronic coherence contributes to photocurrent generation in organic semiconductor heterojunction diodes. *Nat. Commun.* **11** 617 (2020).

17. Athanasopoulos S, Bässler H, Köhler A. Disorder vs Delocalization: Which Is More Advantageous for High-Efficiency Organic Solar Cells? *J. Phys. Chem. Lett.* **10** 7107-7112 (2019).

18. Song Y, Clafton SN, Pensack RD, Kee TW, Scholes GD. Vibrational coherence probes the mechanism of ultrafast electron transfer in polymer–fullerene blends. *Nat. Commun.* **5** 4933 (2014).

19. Tilluck RW, Mohan T. M N, Hetherington CV, Leslie CH, Sil S, Frazier J*, et al.* Vibronic Excitons and Conical Intersections in Semiconductor Quantum Dots. *J. Phys. Chem. Lett.* **12** 9677-9683 (2021).

20. Debnath T, Sarker D, Huang H, Han Z-K, Dey A, Polavarapu L*, et al.* Coherent vibrational dynamics reveals lattice anharmonicity in organic–inorganic halide perovskite nanocrystals. *Nat. Commun.* **12** 2629 (2021).

21. Shen S-W, Wei Y-C, Fu F-Y, Chou K-J, Wang S-F, Fu L-W*, et al.* Interlayer Charge Transfer Coupled with Acoustic Phonon in Organic/Inorganic van der Waals Stacked Heterostructures: Self-Assembled Pt(II) Complex on a PtSe2 Monolayer. *J. Phys. Chem. C* **124** 25538-25546 (2020).

22. Cassette E, Pensack RD, Mahler B, Scholes GD. Room-temperature exciton coherence and dephasing in two-dimensional nanostructures. *Nat. Commun.* **6** 6086 (2015).

23. Quan LN, Park Y, Guo P, Gao M, Jin J, Huang J*, et al.* Vibrational relaxation dynamics in layered perovskite quantum wells. *Proc. Natl. Acad. Sci. U.S.A.* **118** e2104425118 (2021).

24. Thouin F, Valverde-Chávez DA, Quarti C, Cortecchia D, Bargigia I, Beljonne D*, et al.* Phonon coherences reveal the polaronic character of excitons in two-dimensional lead halide perovskites. *Nat. Mater.* **18** 349-356 (2019).

25. Falke SM, Rozzi CA, Brida D, Maiuri M, Amato M, Sommer E*, et al.* Coherent ultrafast charge transfer in an organic photovoltaic blend. *Science* **344** 1001-1005 (2014).

26. Brédas J-L, Sargent EH, Scholes GD. Photovoltaic concepts inspired by coherence effects in photosynthetic systems. *Nat. Mater.* **16** 35-44 (2017).

27. Alvertis Antonios M, Barford W, Bourne Worster S, Burghardt I, Datta A, Dijkstra A*, et al.* Quantum coherence in complex environments: general discussion. *Faraday Discuss.* **221** 168-201 (2020).

28. Wei Y-C, Wang SF, Hu Y, Liao L-S, Chen D-G, Chang K-H*, et al.* Overcoming the energy gap law in near-infrared OLEDs by exciton–vibration decoupling. *Nat. Photonics* **14** 570-577 (2020).

29. Lu C-H, Tsou Y-J, Chen H-Y, Chen B-H, Cheng Y-C, Yang S-D*, et al.* Generation of intense supercontinuum in condensed media. *Optica* **1** 400-406 (2014).

30. Lu C-H, Wu W-H, Kuo S-H, Guo J-Y, Chen M-C, Yang S-D*, et al.* Greater than 50 times compression of 1030 nm Yb:KGW laser pulses to single-cycle duration. *Opt. Express* **27** 15638-15648 (2019).

31. Tamming RR, Lin C-Y, Hodgkiss JM, Yang S-D, Chen K, Lu C-H. Single 3.3 fs multiple plate compression light source in ultrafast transient absorption spectroscopy. *Sci. Rep.* **11** 12847 (2021).

32. Tuong Ly K, Chen-Cheng R-W, Lin H-W, Shiau Y-J, Liu S-H, Chou P-T*, et al.* Near-infrared organic light-emitting diodes with very high external quantum efficiency and radiance. *Nat. Photonics* **11** 63-68 (2017).

33. Wang SF, Yuan Y, Wei Y-C, Chan W-H, Fu L-W, Su B-K*, et al.* Highly Efficient Near-Infrared Electroluminescence up to 800 nm Using Platinum(II) Phosphors. *Adv. Funct. Mater.* **30** 2002173 (2020).

34. Wang S-F, Su B-K, Wang X-Q, Wei Y-C, Kuo K-H, Wang C-H*, et al.* Polyatomic molecules with emission quantum yield > 20% enable efficient Organic Light Emitting Diodes in the NIR(II) window. *Nat. Photonics* just accepted (2022).

35. van der Veen RM, Cannizzo A, van Mourik F, Vlček A, Chergui M. Vibrational Relaxation and Intersystem Crossing of Binuclear Metal Complexes in Solution. *J. Am. Chem. Soc.* **133** 305-315 (2011).

36. Haldrup K, Levi G, Biasin E, Vester P, Laursen MG, Beyer F*, et al.* Ultrafast X-Ray Scattering Measurements of Coherent Structural Dynamics on the Ground-State Potential Energy Surface of a Diplatinum Molecule. *Phys. Rev. Lett.* **122** 063001 (2019).

37. Iwamura M, Fukui A, Nozaki K, Kuramochi H, Takeuchi S, Tahara T. Coherent Vibration and Femtosecond Dynamics of the Platinum Complex Oligomers upon Intermolecular Bond Formation in the Excited State. *Angew. Chem. Int. Ed.* **59** 23154-23161 (2020).

38. Kim P, Valentine AJS, Roy S, Mills AW, Chakraborty A, Castellano FN*, et al.* Ultrafast Excited-State Dynamics of Photoluminescent Pt(II) Dimers Probed by

a Coherent Vibrational Wavepacket. *J. Phys. Chem. Lett.* **12** 6794-6803 (2021).

39. Kim P, Kelley MS, Chakraborty A, Wong NL, Van Duyne RP, Schatz GC*, et al.* Coherent Vibrational Wavepacket Dynamics in Platinum(II) Dimers and Their Implications. *J. Phys. Chem. C* **122** 14195-14204 (2018).

40. Cho S, Mara MW, Wang X, Lockard JV, Rachford AA, Castellano FN*, et al.* Coherence in Metal−Metal-to-Ligand-Charge-Transfer Excited States of a Dimetallic Complex Investigated by Ultrafast Transient Absorption Anisotropy. *J. Phys. Chem. A* **115** 3990-3996 (2011).

41. Trebino R. *Frequency-resolved optical gating : the measurement of ultrashort laser pulses*. Kluwer Academic: Boston, 2000.

42. Trebino R, DeLong KW, Fittinghoff DN, Sweetser JN, Krumbügel MA, Richman BA*, et al.* Measuring ultrashort laser pulses in the time-frequency domain using frequency-resolved optical gating. *Rev. Sci. Instrum.* **68** 3277-3295 (1997).

43. Kohl FR, Grieco C, Kohler B. Ultrafast spectral hole burning reveals the distinct chromophores in eumelanin and their common photoresponse. *Chem. Sci.* **11** 1248-1259 (2020).

44. Chen B-H, Su J-X, Guo J-Y, Chen K, Chu S-W, Lu H-H*, et al.* Double-Pass Multiple-Plate Continuum for High-Temporal-Contrast Nonlinear Pulse Compression. *Front. Photon.* **3** 937622 (2022).

45. Lejman M, Vaudel G, Infante IC, Gemeiner P, Gusev VE, Dkhil B*, et al.* Giant ultrafast photo-induced shear strain in ferroelectric BiFeO3. *Nat. Commun.* **5** 4301 (2014).

46. Shih HC, Chen LY, Luo CW, Wu KH, Lin JY, Juang JY*, et al.* Ultrafast thermoelastic dynamics of HoMnO3 single crystals derived from femtosecond optical pump–probe spectroscopy. *New J. Phys.* **13** 053003 (2011).

47. Barclay MS, Huff JS, Pensack RD, Davis PH, Knowlton WB, Yurke B*, et al.* Characterizing Mode Anharmonicity and Huang–Rhys Factors Using Models

of Femtosecond Coherence Spectra. *J. Phys. Chem. Lett.* **13** 5413-5423 (2022).

48. Lee G, Kim J, Kim SY, Kim DE, Joo T. Vibrational Spectrum of an Excited State and Huang–Rhys Factors by Coherent Wave Packets in Time-Resolved Fluorescence Spectroscopy. *ChemPhysChem* **18** 670-676 (2017).

49. Englman R, Jortner J. The energy gap law for radiationless transitions in large molecules. *Mol. Phys.* **18** 145-164 (1970).

50. Dlott DD, Fayer MD. Shocked molecular solids: Vibrational up pumping, defect hot spot formation, and the onset of chemistry. *J. Chem. Phys.* **92** 3798-3812 (1990).

51. Tong CC, Hwang KC. Enhancement of OLED Efficiencies and High-Voltage Stabilities of Light-Emitting Materials by Deuteration. *J. Phys. Chem. C* **111** 3490-3494 (2007).

52. Bae HJ, Kim JS, Yakubovich A, Jeong J, Park S, Chwae J*, et al.* Protecting Benzylic C H Bonds by Deuteration Doubles the Operational Lifetime of Deep-Blue Ir-Phenylimidazole Dopants in Phosphorescent OLEDs. *Advanced Optical Materials* **9** 2100630 (2021).

53. Li W, Wu A, Fu T, Gao X, Wang Y, Xu D*, et al.* Improved Efficiency and Stability of Red Phosphorescent Organic Light-Emitting Diodes via Selective Deuteration. *J. Phys. Chem. Lett.* **13** 1494-1499 (2022).

54. Spies JA, Neu J, Tayvah UT, Capobianco MD, Pattengale B, Ostresh S*, et al.* Terahertz Spectroscopy of Emerging Materials. *J. Phys. Chem. C* **124** 22335-22346 (2020).

55. McIntosh AI, Yang B, Goldup SM, Watkinson M, Donnan RS. Terahertz spectroscopy: a powerful new tool for the chemical sciences? *Chem. Soc. Rev.* **41** 2072-2082 (2012).

56. Frisch MJ, Trucks GW, Schlegel HB, Scuseria GE, Robb MA, Cheeseman JR, *et al.* Gaussian 16 Rev. C.01. Wallingford, CT; 2016.

57. Lu T, Chen F. Multiwfn: A multifunctional wavefunction analyzer. *J. Comput. Chem.* **33** 580-592 (2012).

58. Neese F. Software update: the ORCA program system, version 4.0. *WIREs Computational Molecular Science* **8** e1327 (2018).

59. Halder M, Datta S, Bolel P, Mahapatra N, Panja S, Vardhan H*, et al.* Reorganization energy and Stokes shift calculations from spectral data as new efficient approaches in distinguishing the end point of micellization/aggregation. *Analytical Methods* **8** 2805-2811 (2016).

60. Mertz EL, Krishtalik LI. Low dielectric response in enzyme active site. *Proc. Natl. Acad. Sci. U.S.A.* **97** 2081-2086 (2000).

61. Jordanides XJ, Lang MJ, Song X, Fleming GR. Solvation Dynamics in Protein Environments Studied by Photon Echo Spectroscopy. *J. Phys. Chem. B* **103** 7995-8005 (1999).

Methods

Computational method. The tetrameric **4H** was simulated using the established packing model. We applied the Gaussian 16 program[56] to perform density functional theory (DFT) calculations at the hybrid functional PBE1PBE-D3/LANL2DZ (for Pt atoms) and ωB97XD/6-31 g(d) (for H, C, N, F atoms) levels. According to the GIXD packing structures, we adopt the GIXD-resolved packing structure as the initial structure in the optimization process. The natural transition orbitals are calculated by the Multiwfn program.[57] The spin-orbit couplings are calculated using the ORCA program,[58] and the results are shown in Tables S1 and S2.

Light source. The measurements were performed using a commercial Yb:KGW laser system (Pharos, Light Conversion) with a central wavelength of 1030 nm, an average power of 2.5 W, a repetition rate of 3.125 kHz, a pulse energy of 800 μJ and a pulse duration of 190 fs. Two identical pulses were produced with a low-GDD 50/50 beam splitter and passed through our designed nonlinear compressor using a previously reported technique, namely, multiple plate compression (MPC).[29, 30] For this experiment, a high-pass filter with a cut-off wavelength of 980 nm was applied. The final spectra of these two pulse replicas spanned from 550 nm to 980 nm, as shown in the grey area of Fig. S1a. Pulse compression was achieved with 8 chirped mirror bounces (Ultrafast Innovation), thus removing the material dispersion introduced by the optics before the sample. The compressed pulses had an FWHM duration of 3.2 fs and were characterized at the sample position with a polarization-gating frequency-resolved optical gating (PG-FROG), as shown in Fig. S1.

High-speed shot-to-shot transient absorption setup. The schematic setup of our ultrafast transient absorption measurement system is depicted in Fig. S2. The pump pulse was modulated by a laser-triggered mechanical chopper modulating at half the laser repetition rate (1.5625 kHz). Tunable colour filters (combination of high- and low-pass filters) were employed to fine-tine the pumping bandwidth and central wavelength. A broadband half-wave plate and wire-grid polarizer were used to precisely control the excitation power and ensure that no nonlinear effects were introduced. The delay time (relative to the pump pulse) of the probe pulse was adjusted by a linear translation stage (DL325, Newport) that supports a delay range up to ~ 2.2 ns. The pump and probe beams were both focused on the sample in a noncollinear manner with a cross-angle of 5 degrees. Different focusing conditions were chosen for pump and probe pulses to ensure that the focused pump spot size (~67.7 μm) was slightly larger than the focused probe spot size (~27.3 μm) and that the probed region was uniformly excited. After the pulses passed through the sample, the transmitted probe pulse was spatially separated and guided into our designed spectrometer, which includes a high-speed linear array camera (Glaz Linescan-I-Gen2, Synertronic with S12198-512Q CMOS, Hamamatsu) to ensure that each probe pulse is captured. Since the pump pulses are modulated at half of the repetition rate, the spectral difference between every two probe shots (one sees the pump, while the other does not) provides the ΔT/T signal.

Tunability of the excitation bandwidth and pulse duration. The bandwidth and pulse duration tunability of our ultrafast transient absorption system is essential for performing the measurements discussed in this paper. In general, the duration of the pump pulse is measured by an intensity autocorrelation (IA) or second-harmonic frequency-resolved optical gating (SHG-FROG). However, these measurements provide only indirect results and may fail to measure durations less than 10 fs due to phase-matching bandwidth limitations. Thus, we use a polarization-gating frequency-resolved optical gating (PG-FROG) to acquire the pulse information used in our measurements and present the results in Figs. S4 and S5.

Fitting of the beating signal. To quantify the frequency of vibrational coherence in the TA measurements, the oscillatory components *f*(*t*) were fit using Eq. 2:

$$f(t) = A_1 \sin(2\pi t/T + \varphi)\, e^{(-t/\tau_1)} + A_2 e^{(-t/\tau_2)} + B_0, \qquad (2)$$

where A_1 is an oscillation amplitude scaling constant, τ_1 is the dephasing time, T is the period, φ is the phase shift, A_2 is a prefactor of the exponential decay, B_0 is the baseline signal and τ_2 is the decay lifetime of the incoherent excited-state deactivation processes. The time trace at 575 nm can be determined with Eq. 1 using values of $\tau_1 = \tau_d = 534$ fs, $T = 1.063$ ps and $\tau_2 = 916$ fs. The time trace at 700 nm can be determined with Eq. 1 using $\tau_1 = \tau_d = 534$ fs, $T = 0.977$ ps and $\tau_2 = 4.234$ ps.

Validity of Equation 1. According to a previous report,[49] Eq. (1) is valid when $\lambda/\bar{\omega} >> 1$. To verify whether the aggregated Pt(II) complexes met this criterion, we estimated the λ and $\bar{\omega}$ values of aggregated **4H**. According to the relation between the Stokes shift of the steady-state spectra (Fig. 1b) and the reorganization energy,[59-61] we determined that $\lambda \approx 2627$ cm^{-1}. Based on the definition of $\bar{\omega}$ and Fig. S14, we calculated $\bar{\omega} \approx 111$ cm^{-1}. Based on the above estimation, we obtained $\lambda/\bar{\omega} \approx 23.67$, which satisfies the validity criteria for Eq. (1).

Acknowledgements

This research was supported by funding from the National Science and Technology Council (NSTC), National Taiwan University, National Tsing Hua University, Academia Sinica, the Innovation and Technology Fund (ITS/196/20), and Victoria University of Wellington.

Author contributions

Y.C. designed and synthesised all Pt(II) complexes. Y.-C.W., R.-S.Y. and H.-W.H. performed the optical measurements. B.-H.C., C.-H. L, K.C, J.-X.S. and S.-D.Y. developed the MPC-TAS system. Y.-C.W. and L.-Y.H. performed the simulations and calculations. Y.-C.W., K.C. and P.-T.C. discussed and interpreted the spectroscopic data. Y.-C.W., B.-H.C., C.-H.L., S.-D.Y. and P.-T.C. prepared the manuscript. All authors discussed the results and contributed to the paper.

Additional information

Supplementary information can be obtained at www.nature.com/naturephotonics. Reprints and permission information are available online at http://www.nature.com/reprints.

Competing financial interests

The authors declare no competing financial interests.

Supplementary Files

This is a list of supplementary files associated with this preprint. Click to download.

- VCSI20220930final.pdf